

Modeling and Statistical Characterization of Large-Scale Automotive Radar Networks

Mohammad Taha Shah, Gourab Ghatak, Ankit Kumar, and Shobha Sundar Ram

Abstract—The impact of discrete clutter and co-channel interference on the performance of automotive radar networks has been studied using stochastic geometry, in particular, by leveraging two-dimensional Poisson point processes (PPPs). However, such characterization does not take into account the impact of street geometry and the fact that the location of the automotive radars are restricted to the streets as their domain rather than the entire Euclidean plane. In addition, the structure of the streets may change drastically as a vehicle moves out of a city center towards the outskirts. Consequently, not only the radar performance change but also the radar parameters and protocols must be adapted for optimum performance. In this paper, we propose and characterize line and Cox process-based street and point models to analyze large-scale automotive radar networks. We consider the classical Poisson line process (PLP) and the newly introduced Binomial line process (BLP) model to emulate the streets and the corresponding PPP-based Cox process to emulate the vehicular nodes. In particular, the BLP model effectively considers the spatial variation of street geometry across different parts of the city. We derive the effective interference set experienced by an automotive radar, the statistics of distance to interferers, and characterize the detection probability of the ego radar as a function of street and vehicle density. Finally, leveraging the real-world data on urban streets and vehicle density across different cities of the world, we present how the radar performance varies in different parts of the city as well as across different times of the day. Thus, our study equips network operators and automotive manufacturers with essential system design insights to plan and optimize automotive radar networks.

Index Terms—Stochastic geometry, Automotive radar, Poisson line processes, Poisson line Cox process, Binomial line process, Binomial line Cox process.

I. INTRODUCTION

Millimeter-wave automotive radars have proliferated on roads to support advanced driver assistance systems to reduce road accidents and improve passenger comfort and efficiency. These radars support several important applications, including automatic cruise control, obstacle detection, and blind spot detection [1], [2]. A comprehensive introduction to automotive radar is presented in [3]–[6]. Based on the advantages these radars offer, it is predicted that every car on the road will carry at least one radar in the near future. However, the downside to this development is that as more vehicles get equipped with radars, mutual interference between them will begin to limit the performance since they occupy the

same frequency band [7], [8]. Several potential solutions for mitigating interference have been suggested based on resource-based multiplexing in time, frequency, space, and modulation, or adaptive beamforming. However, in order to design and develop effective interference-mitigation solutions, researchers require accurate and tractable models for automotive radar networks. Currently, the state-of-the-art statistical models of automotive radar networks are based on simplistic assumptions of the locations of vehicular nodes, e.g., assuming them to be located only on highways [9], [10]. We bridge this gap in this paper by introducing novel models that not only accurately emulate the urban street geometry but are also remarkably tractable so as to enable initial network planning.

A. Related Work

A plethora of recent works have come up on automotive radar networks, which focus on modeling and characterization of automotive radar interference [9]–[15]. The authors of [11] modeled how the interference between two radars operating in overlapping frequency bands significantly degraded target detection and tracking. In [12], the authors showed that mutual interference between automotive radars with frequency-modulated continuous waveforms (FMCW) causes ghost targets and lower sensitivity. Schipper *et al* [13] considered radar interference when modeling vehicle distribution along a roadway based on traffic flow patterns.

More recently, stochastic geometry (SG) techniques have been exploited to characterize automotive radar interference while tackling the diversity of radar distributions [9], [14], [16]. SG models are essential for accurately evaluating system performance and the efficacy of mitigation strategies. Improved models result in more accurate assessments, facilitating the development of more efficient solutions. Likewise, the advantage of the SG-based analytical framework is that diverse spatial conditions can be explored at a fraction of the computational cost and time associated with system-level Monte Carlo simulations or measurement data collection. For instance, the authors in [9] considered Poisson point process (PPP) to model the distribution of vehicular automotive radars and estimate the mean signal-to-interference ratio (SIR) for radar detection metrics. Munari *et al.* [14] used the strongest interferer approximation to determine the radar detection range and false alarm rate. The radar detection probability was investigated in [16] while accounting for fluctuating radar cross-sections (RCS) of targets with Swerling-I and Chi-square models to provide more accurate and intuitive results than constant RCS models. The above-mentioned work mainly focuses on two-lane scenarios. For a multi-lane scenario, authors in [15]

M.T. Shah and A. Kumar are with the Bharti School of Telecommunication Technology and Management, IIT Delhi, New Delhi, India, 110016; Email: {tahashah, bsy227531}@dbst.iitd.ac.in. G. Ghatak is with the Department of Electrical Engineering, IIT Delhi, New Delhi, India, 110016; Email: gghatak@ee.iitd.ac.in. S. S. Ram is with the Department of Electronics and Communication Engineering, IIIT Delhi, New Delhi, India, 110020; Email: shobha@iiitd.ac.in

addressed the interference characterization using a marked point process model. A more recent method used the Matern hard-core process (MHCP) [17], [18] accounting for the size of the vehicles and the amount of space they require on the road to provide a more realistic model of interference.

With better modeling of automotive radar networks, several techniques have been devised for mitigating automotive radar interference in the following work. Using a PPP model, the study in [19] evaluated interference scenarios and proposes a centralized framework leveraging vehicle-to-everything (V2X) communication to allocate spectrum resources and minimize radar interference. Likewise, authors in [20] introduce a VANET-assisted scheme that employs a TDMA-based MAC protocol to coordinate radar spectrum access among vehicles, enhancing interference mitigation. Aydogdu *et al.* [21] proposed a distributed networking protocol for wireless radar control and interference mitigation. In [22], authors introduced random frequency division multiplexing (RFD), frequency hopping (FH), and an adaptive frequency hopping with phase modulation (AFH-PM) to mitigate interference in an MHCP vehicle distribution in two-lane and multi-lane scenarios.

SG analytics have also been extended to other automotive radar scenarios for modeling the impact of clutter on radar detection performance [23]–[27]. In [23], the authors modeled the discrete clutter scatterers in radar scenarios and estimated the radar detection metrics using a PPP model. They further utilized this framework in [24] to optimize pulse radar parameters for maximizing the probability of detection. They investigated the bi-static radar framework for terrestrial [25] and space-based scenarios in [27] and further extended the model to optimize the time resource management between radar and communications in integrated sensing and communication systems [26].

B. Motivation

Previous studies on SG-based spatial networks have not considered complex real-world urban environments. For instance, in real-life scenarios, automotive radars are likely to be randomly located on streets rather than off streets. Therefore, the prior assumption that an interfering radar could be randomly located anywhere near the ego radar is incorrect. In this work, we factor in the structure of city streets (downtown versus suburban city areas) and the time of the day (peak versus off-peak hours) to analyze the performance of automotive radar networks. Specifically, we explore the impact of street geometry on radar interference using line processes, which are random collections of lines in a two-dimensional Euclidean plane. Further, the distribution of cars on the street is modeled as a point process with the lines as their domain. Together, this forms a doubly stochastic Cox model of automotive radars to study the effect of interference on the detection performance of an ego radar. Researchers have explored Cox models in modelling cellular and V2X networks [28]–[30]. In [10], the authors presented a fine-grained radar detection analysis highlighting optimal channel access methods. However, the work primarily focused on a specific highway scenario, potentially limiting its generalizability across diverse real-life scenarios.

In this work, we characterize two SG models designed for two different network contexts: (i) the Poisson line Cox process (PLCP) model, which caters to analyzing dense city centers and smaller regions in the city, and (ii) the binomial line Cox process (BLCP) model that jointly takes into account the city center and outskirts, thereby providing a more holistic view of the city. Indeed, the PLCP model is obtained in the asymptotic limit of the BLCP. Then, for both models, we derive the framework to study the analytical performance of a typical ego radar in terms of detection probability for real-world cities.

C. Organization and Contributions

The key contributions of our work are as follows:

- First, leveraging the PLCP and the BLCP frameworks, we model complete street networks for automotive radars. By considering both the homogeneity of city centers and the inhomogeneity of suburban regions, these models offer a comprehensive approach to understanding the performance of automotive radar networks under varying spatial distributions. Ours is the first work that extends the simplistic two-lane model for studying automotive radars to a more realistic multi-street scenario.
- Then, we define the interfering sets for the models and derive the distance statistics between the interfering radars and ego radar. Then, based on the derived interfering set, we characterize the statistics of the interference experienced by the ego radar. This enables us to derive the radar detection probability and study the impact of the density of the streets, the vehicular density, and the beamwidth on the detection performance of the ego radar. The results provide key insights for automotive manufacturers and network operators aiming to optimize radar system designs under practical conditions.
- Finally, our study leverages real-world street network data from multiple cities to validate the proposed models and examine radar performance across different urban layouts. We, specifically, account for the urban road density in these cities and the car density on the roads during peak and off-peak hours.

The overall paper is organized as follows. In the following section II, we define the street geometry models and channel model. In Section III, we define the set of points falling within a radar sector and, consequently, the interfering vehicles set. Following which we derive the maximum and minimum distance between the ego radar and interfering radar present on i^{th} line. Finally we derive the detection probability in Section IV, and plot various results in section V against various system parameters in accordance with real-world road and traffic network parameters.

D. Notations

To differentiate the notations between the two Cox process models, we will use subscript of ‘ $k = P$ ’ for PLCP and ‘ $k = B$ ’ for BLCP models. For example, line processes are identified using calligraphic letters such as \mathcal{P} , thus \mathcal{P}_P denotes

Notation	Description
\mathcal{P}_P	Poisson line process
λ_L	Intensity of PLP
\mathcal{P}_B	Binomial line process
Φ_P	Poisson line Cox process
Φ_B	Binomial line Cox process
L_i	i -th line of a Poisson line process (PLP) or binomial line process (BLP)
Φ_{L_i}	Poisson point process on i -th line of a PLP or BLP
λ	Intensity of Φ_{L_i}
k	$k = P$ represents PLP/PLCP, and $k = B$ represents BLP/BLCP
\mathcal{D}_k	Generating domain of k line process
R	Distance of ego radar to target
Ω	Half power beamwidth of automotive radars
\mathbf{a}	Boresight direction of automotive radars
n_B	Number of lines of the BLP \mathcal{P}_B
R_g	Radius of circle in which BLP \mathcal{P}_B is restricted
$\mathcal{C}((0,0), R_g)$	A disk/circle of radius R_g centered at $(0,0)$
r_0	Distance of ego radar from origin
u_i	Intersection distance of i -th line from origin
d_i	Intersection distance of i -th line from ego radar
$\ w_{k,i}\ $	Distance between ego radar and interfering radars present on L_i
R_k	Maximum distance between ego radar and interfering radar
$\mathcal{R}_{(x,y),k}^+$	Radar Sector generated by any radar point for axis vector $\mathbf{a} = (0,1)$
Φ_k^I	Set of interfering Cox points for PLCP/BLCP
$h_{\mathbf{w}_k}$	Fading power
ξ_k	SINR received at the ego radar
γ	SINR threshold
$p_{D,k}(\gamma)$	Detection probability at threshold γ

Table I: Summary of notations used in the paper.

PLP and \mathcal{P}_B denotes BLP. Likewise, point processes are identified using the symbol Φ_P for PLCP, and Φ_B for BLCP. A BLP usually consists of n_B lines. Probability operators are represented by \mathbb{P} and expectation by \mathbb{E} . A complete list of important notations is presented in Table I.

II. SYSTEM MODEL

A. Network Geometries

If we consider a snapshot of road geometries of some of the biggest cities in the world, e.g., see New Delhi in Fig. 1 (a) and Paris, Washington, and Johannesburg in the first column of Table II, we observe a random distribution of streets, both in terms of density and orientation. From the perspective of an ego radar, there can be a significant variation in street geometry and vehicle density at any time. Therefore, instead of considering each distribution of automotive radars on the roads as a separate scenario, we treat them as an instance of an underlying spatial stochastic process. Accordingly, we model the road network as a line process. In particular, we consider two models. First, we consider a network of streets as a homogeneous PLP, typical of road geometries within a small area/district within a city. The second model considers a network of streets as inhomogeneous BLP with greater road density at the center (city centers/downtown) and lower road density at the peripherals (suburbs).

1) *PLCP*: We consider a network of streets modeled as a homogeneous PLP, $\mathcal{P}_P = \{L_1, L_2, \dots\}$, i.e., a stochastic set of lines in the two-dimensional Euclidean $x-y$ plane. Any line, L_i , of \mathcal{P}_P is uniquely characterized by its distance r_i from the origin and the angle θ_i between the normal and the x -axis as shown in Fig. 3. The pair of parameters (θ_i, r_i) corresponds to a point, \mathbf{q}_i , in the representation space $\mathcal{D}_P \equiv$

$[0, 2\pi) \times (0, \infty)$ which is an open cylinder, and is called the domain set of \mathcal{P}_P . Thus, there is a one-to-one correspondence between $\mathbf{q}_i, i = 1 : I$ in \mathcal{D}_P and the lines, $L_i, i = 1 : I$ in \mathbb{R}^2 . The number of generating points, I , in any $S \subset \mathcal{D}_P$ follows the Poisson distribution with parameter $\lambda_L|S|$, where $|S|$ represents the Lebesgue measure of S . The parameter $\lambda_L|S|$ represents the urban road density, which varies from city to city and within a city from downtown to suburban areas. Our analysis for PLP focuses on the perspective of an automotive radar mounted on a typical ego vehicle located at the origin of the two-dimensional plane, as shown in Fig. 1 (b). The radars have a half-power beamwidth of Ω , and the target is assumed to be located at a distance of R from the radar on the same street within the main beam of the ego radar.

We assume that the street with the ego radar and target is present on is represented by L_0 with parameters $(\theta_0, r_0) = (0, 0)$. As per the Palm distribution of a PLP, the statistics of the rest of the process remain unaltered [31]. The locations of the vehicles with mounted radars on the L_i^{th} street follow a one-dimensional PPP, Φ_{L_i} , with intensity λ , that represents the vehicular density. Naturally, we can use a higher λ to model the traffic conditions during peak hours compared to off-peak hours. The PPP of vehicles on any street is assumed to be independent of the corresponding distributions on the other streets. Hence, the complete distribution of the vehicles (other than the ego vehicle/radar) in the space is a homogeneous PLCP Φ , on the domain \mathcal{P}_P where the PLCP is defined as $\Phi_P = \bigcup_{L_i \in \mathcal{P}_P} \Phi_{L_i}$.

Figure 1(a) shows one realization of the PLCP, where the ego radar is present at the origin on the road aligned along the y axis. The other streets in the neighborhood are shown as lines in the figure. The PLCP points representing automotive

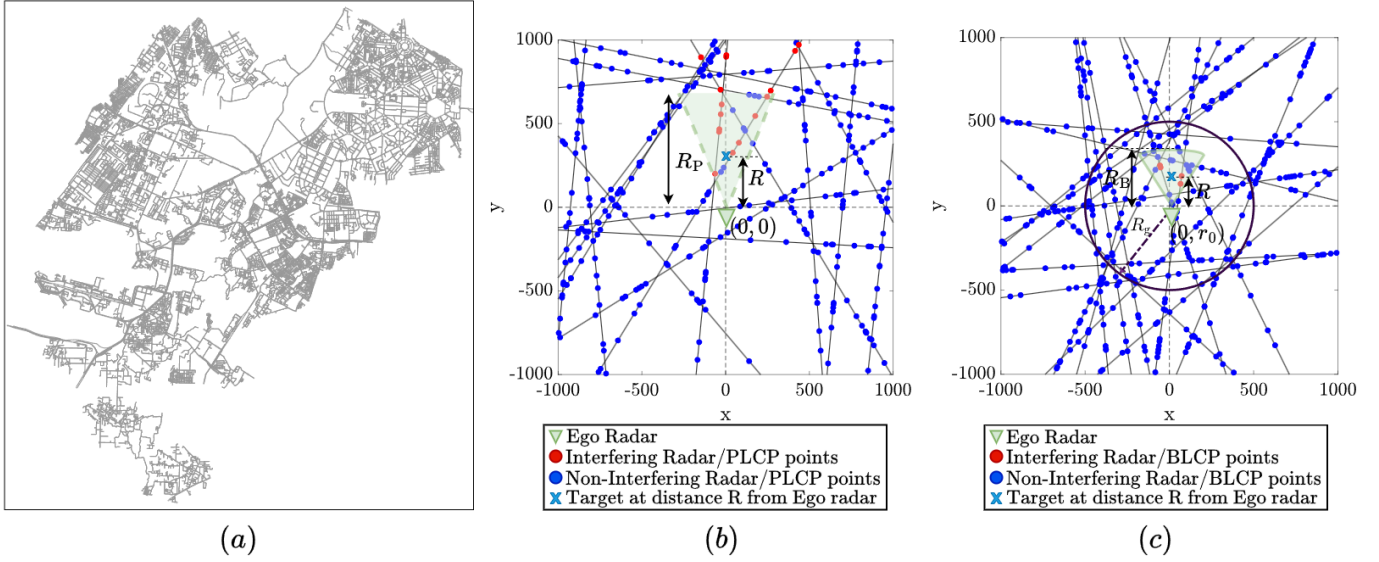


Fig. 1. (a) Road map of New Delhi city, (b) A realization of PLCP having $\lambda_L = 0.005 \text{ m}^{-2}$ and $\lambda = 0.005 \text{ m}^{-1}$, with ego radar present at origin, and (c) A realization of BLCP having $n_B = 50$ and $\lambda = 0.005 \text{ m}^{-1}$, with ego radar present at $(0, r_0)$.

radars are situated on these streets, and they may or may not contribute to the interference experienced by the ego-radar. This will be formally characterized subsequently. The ego radar will experience interference if and only if both the ego radar and interfering radar fall into each other's radar sectors simultaneously. To model the interference from vehicles from the opposite side of the road, we consider on line L_0 the location of vehicles follows a one-dimensional PPP having the same intensity as the remaining lines. Therefore, the overall spatial stochastic process is represented as Φ_{P_0} , which as per the Palm conditioning, is the superposition of Φ_P , and an independent 1D PPP on line L_0 , i.e., $\Phi_{P_0} = \Phi_P \cup \Phi_{L_0}$.

2) *BLCP*: Contrary to a PLP, a BLP \mathcal{P}_B is a finite collection of lines, i.e., n_B in the two-dimensional Euclidean plane, defined as, $\mathcal{P}_B = \{L_1, L_2, \dots, L_{n_B}\}$. Each line of \mathcal{P}_B corresponds to a point in the binomial point process (BPP). The set \mathcal{P}_B is generated by points on a finite cylinder $\mathcal{D}_B := [0, \pi) \times [-R_g, R_g]$, which is the generating set of \mathcal{P}_B . The point on the cylinder is denoted by $(\theta_i, r_i) \in \mathcal{D}_B$ and corresponds to a line $L_i \in \mathcal{P}_B$. Thus, in Euclidean space, the generating points of the lines are restricted to the disk $\mathcal{C}((0, 0), R_g)$. The normal to the line L_i is formed by drawing a line segment from the origin to (θ_i, r_i) . It is important to note that due to the finite domain of the generating set, the resulting line process is non-homogeneous in the Euclidean plane. Like PLCP, we define on each line L_i of \mathcal{P}_B , an independent 1D PPP Φ_{L_i} with intensity λ . A BLCP Φ_B , is the collection of all such points on all lines of the BLP, i.e., $\Phi_B = \bigcup_{i=1}^{n_B} \Phi_{L_i}$.

Thus, BLCP like PLCP is a Cox process of random points defined on random lines. Due to the underlying inhomogeneity, the statistics of the BLP cannot be characterized by perspective at just one typical point, such as one located at the origin. The isotropic structure of BLCP implies that its characteristics, when observed from a specific point, are determined by the distance from the origin rather than the orientation of the point. A test point at $(0, r_0)$ is considered without limiting

our generalization. Now, from the palm perspective of the BLCP [32], conditioning on a point to be located at $(0, r_0)$ in a BLCP is the same as taking into consideration an atom at $(0, r_0)$, and a 1-D PPP on a line L_0 that passes through $(0, r_0)$. Thus, the reduced stochastic process consists of $n_B - 1$ lines defined in the same domain. Vehicles from the opposite side of the road are modeled as 1D PPP on line L_0 having the same intensity as the remaining lines. The overall spatial stochastic process is represented as Φ_{B_0} .

Figure 1(c) shows an instance of the BLCP, where the ego radar is located at the $(0, r_0)$, and the disk of radius R_g which restricts the generating point of lines. Besides, we see a beam of green color of radius R_B , which is the maximum range of the ego radar. The remaining BLCP points represent automotive radars, which may or may not cause interference. The red dots signify the interfering radars, while the blue dots represent the non-interfering radar. For the ego radar to experience interference, both the ego radar and interfering radar must be within a distance of R_B from each other simultaneously. Similar to PLCP, we assume that each radar has a half-power beamwidth of Ω , and the target is located at a distance of R from the radar on the same street.

B. SIR and Channel Model

Let the transmit power be P and the path-loss exponent be α . The target is at a distance R from the ego radar and is assumed to have a Swerling-I fluctuating radar cross-section, σ_c , with a mean of $\bar{\sigma}$ [33]. Let G_t be the gain of the transmitting antenna and A_e the effective area of the receiving antenna aperture. Then, the ego radar receives the reflected signal power from the target vehicle with strength

$$S = \gamma \sigma_c P R^{-2\alpha} \quad (1)$$

where $\gamma = \frac{G_t}{(4\pi)^2} A_e$. Let the coordinates of any PLCP point/interfering radar in the Euclidean plane be denoted by $\mathbf{w}_P = (x, y)$, such that $x \cos \theta_i + y \sin \theta_i = r_i$ for

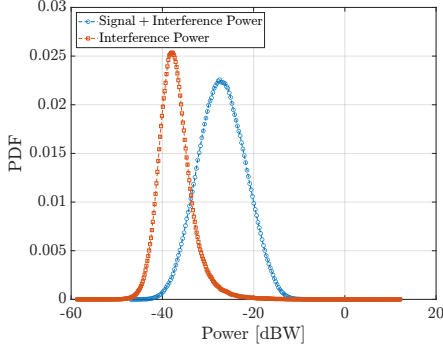


Fig. 2. PDF of signal + interference power and only interference power received at ego radar, if the target is at a distance uniformly distributed between 5 to 15 m, $\Omega = 30^\circ$, $\lambda_L = 0.01 \text{ m}^{-1}$, $\lambda = 0.05 \text{ m}^{-1}$, and transmit power is 1 dB.

$(\theta_i, r_i) \in \mathcal{D}_P$. Likewise $\mathbf{w}_B = (x, y)$ be the coordinates of any BLCP point/interfering radar, such that $x \cos \theta_i + y \sin \theta_i = r_i$ for $(\theta_i, r_i) \in \mathcal{D}_B$. Due to the mm-wave channel effects, the interfering signals undergo multi-path fading, modeled as a Rayleigh-distributed random variable with parameter 1. Furthermore, the fading gain is assumed to be independent across all radars. The interference at the ego radar for both PLCP and BLCP due to any one interfering radar located at w_k is then given by,

$$\mathbf{I}_k = P\gamma h_{\mathbf{w}_k} \|\mathbf{w}_k\|^{-\alpha}, \quad (2)$$

where $h_{\mathbf{w}_k}$ is the fading power. Now, assuming that all the automotive radars share the same power and gain characteristics, the SIR at the ego radar is

$$\xi_k = \frac{\gamma \sigma_c P R^{-2\alpha}}{N + \sum_{\mathbf{w}_k \in \Phi_k^I} 4\pi\gamma P h_{\mathbf{w}_k} \|\mathbf{w}_k\|^{-\alpha}}, \quad (3)$$

where $k \in \{P, B\}$, and Φ_k^I is the interfering set defined in next section. It is important to note that ξ_B is a function of r_0 . For our analysis of PLCP or BLCP, we make the crucial assumption that the radar has a maximum allowable range or operational range, which we denote as R_k . This implies that the ego radar cannot detect any target beyond the R_k range. In real-world scenarios, the automotive radar can experience blockages from buildings and objects, hampering the radar's detection range. Thus, R_k can also be interpreted as the line-of-sight (LOS) range of the automotive radar. Therefore, we assume that any other radar not inside the R_k range of the ego radar sector will not interfere with the ego radar's detection performance. Thus, the distance between the ego radar and interfering radars is limited, i.e., $\|\mathbf{w}_k\| \leq R_k$.

Let us now illustrate the significance of characterizing the SIR in radar system design. Recall that the traditional metrics for studying radar systems are the probability of detection and the probability of false alarm. The probability of detection refers to the possibility that the sum power of the received signal, interference, and noise exceeds a predetermined threshold for radar detection. On the other hand, the probability of a false alarm is the probability that only the interference and noise reach this threshold without the presence of an actual signal. In Fig. 2, we plot the probability distribution functions (PDF) of the signal plus interference strength received at ego radar,

along with that of only the interference power, using Monte Carlo simulations. For any likelihood ratio-based detection strategy, an appropriate threshold is needed to characterize the detection event. From Fig. 2, the optimal threshold exists at the intersection of two PDFs, which is -33 dB. A larger separation between the two PDFs enables a larger flexibility in selecting the threshold for detection subject to a constraint on the false alarm. Accordingly, in this work, we characterize the performance of the radar network in terms of the cumulative density function (CDF) of the signal-to-interference-plus-noise ratio (SINR) experienced by the ego radar.

III. CHARACTERIZATION OF THE INTERFERENCE PROCESS

We observe from Fig 1 (b) and (c) that all the Cox points do not cause the interference. Instead, interference is caused at the ego radar only when both the ego radar and the interfering radar are simultaneously within each other's radar sectors. For example, in Fig 3, we see the radar sectors (soon to be defined) emitted by four vehicles, namely A, B, C, D, and E. The vehicle A, located at the origin $\mathbf{0}$, represents the ego radar, and its radar sector is depicted in green. The beams of the interfering and non-interfering vehicles are represented by purple and red, respectively. Therefore, ego radar experiences interference only from B and E, and not from C and D. In the subsequent discussion, we characterize the interfering distance and determine its effect on the system performance.

We shall first define the subset of \mathbb{R}^2 defined by the conic beam (henceforth referred to as the radar sector) and then determine the collection of Cox points located within the radar sector formed by the radar beam.

A. Interfering Set

The orientation of the vehicles on the street depends on the generating angle of the street and the direction of their movement. Thus, the boresight direction of any radar on i^{th} line is given by the two unit vectors: \mathbf{a} and $-\mathbf{a}$, where $\mathbf{a} = (-\sin \theta_i, \cos \theta_i)^T$. We see that the parameter of the line L_i , i.e., (θ_i, r_i) , determines the direction of the radar sector. Any point in the Euclidean plane (p, q) lies in the sector if the angle made by the displacement vector between $(p, q) - (x, y)$ and the boresight direction is larger than $\cos \Omega$. Thus, the sector for any radar is uniquely characterized by $\mathcal{R}_{(x,y),k}^+$ and $\mathcal{R}_{(x,y),k}^-$ as a function of (x, y) and Ω . Thus we can define the *closed* interior region of the radar sector for any Cox point of PLCP or BLCP (x, y) in the Euclidean plane as follows:

Definition 1. The radar sector of a radar located at $(x, y) \in \Phi_{k_0}$ such that $x \cos \theta_i + y \sin \theta_i = r_i$ and $(\theta_i, r_i) \in \{\mathcal{D}_k \cup (0, 0)\}$ for boresight direction \mathbf{a} is

$$\begin{aligned} \mathcal{R}_{(x,y),k}^+ &= \left\{ (p, q) \in \mathbb{R}^2 : \frac{((p, q) - (x, y)) \cdot \mathbf{a}}{\|(p, q) - (x, y)\|} > \cos \Omega, \right. \\ &\quad \left. \|(p, q) - (x, y)\| \leq R_k \right\} \\ &= \left\{ (p, q) \in \mathbb{R}^2 : \frac{\cos \theta_i (q - y) - \sin \theta_i (p - x)}{\sqrt{(p - x)^2 + (q - y)^2}} > \cos \Omega, \right. \end{aligned}$$

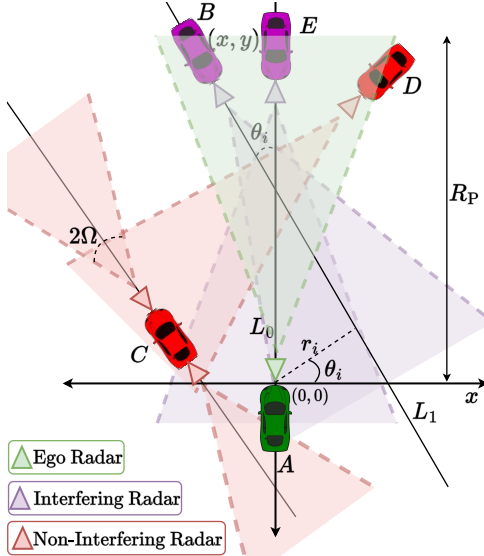


Fig. 3. Illustration of a scenario showing interfering and non-interfering radar sectors w.r.t. ego radar.

$$\left. \sqrt{(p-x)^2 + (q-y)^2} \leq R_k \right\}.$$

And for boresight direction $-\mathbf{a}$,

$$\mathcal{R}_{(x,y),k}^- = \left\{ (p,q) \in \mathbb{R}^2 : \frac{\sin \theta_i (p-x) - \cos \theta_i (q-y)}{\sqrt{(p-x)^2 + (q-y)^2}} > \cos \Omega, \right. \\ \left. ; \sqrt{(p-x)^2 + (q-y)^2} \leq R_k \right\}$$

In case of PLCP, the radar sector formed by ego radar is given for $(\theta_i, r_i) = (0, 0)$, and $(x, y) = (0, 0)$, while as for BLCP $(x, y) = (0, r_0)$. Thus, the radar sector formed by automotive radar is *bounded*.

Example: Figure 3 shows the ego radar sector as $\mathcal{R}_{(0,0),P}^+$ in green color. Here $\mathbf{a} = (0, -1)$. Similarly, on the line L_i , the radar sector, $\mathcal{R}_{(x,y),P}^-$, of an interfering vehicle B , located at $(x, y) \in \Phi_P$ is illustrated by the magenta color. We have also illustrated the two radar sectors of the vehicle C for two boresight vectors, i.e., \mathbf{a} and $-\mathbf{a}$. Thus, the ego radar at any position only experiences interference from PLCP points in its radar sector, and the ego radar is in their radar sector. Furthermore, if the ego radar has \mathbf{a} as the boresight direction, then only the radars with boresight direction $-\mathbf{a}$ can contribute to interference.

The same arguments follow for the BLCP model, with the only difference being the location of ego radar. This makes the analysis of BLCP more involved in a location-dependent framework. We generalize the set of interfering points as:

Definition 2. For any Φ_{k_0} , the set of Cox points Φ_k^I that cause interference at the ego radar is

$$\Phi_k^I = \bigcup_{(x,y) \in \Phi_{k_0}} \left\{ (x, y) : \left(\mathbf{1} \left((0, r) \in \mathcal{R}_{(x,y),k}^+ \right) + \mathbf{1} \left((0, r) \in \mathcal{R}_{(x,y),k}^- \right) \right) \right\}$$

$$\cdot \left(\mathbf{1} \left((x, y) \in \mathcal{R}_{(0,r),k}^+ \right) + \mathbf{1} \left((x, y) \in \mathcal{R}_{(0,r),k}^- \right) \right) = 1 \Big\}.$$

where $\mathbf{1}(\cdot)$ is the indicator function, $\mathcal{R}_{(x,y),k}^+$ is closed interior region of any radar present at (x, y) , and $(0, r)$ is the location of ego radar, and $k \in \{P, B\}$. In the case of $k = P$, the location of ego radar is at the origin, thus $r = 0$, and in BLCP, $r = r_0$.

The above definition outlines the set of interfering automotive radars Φ_k^I , having coordinates (x, y) that cause interference at the ego radar. If ego radar falls within the radar sector of automotive radar present at (x, y) i.e., $\mathbf{1} \left((0, r) \in \mathcal{R}_{(x,y),P}^+ \right) + \mathbf{1} \left((0, r) \in \mathcal{R}_{(x,y),P}^- \right)$, and the automotive radar located at (x, y) falls in the interior region of ego radar i.e., $\mathbf{1} \left((x, y) \in \mathcal{R}_{(0,r),P}^+ \right) + \mathbf{1} \left((x, y) \in \mathcal{R}_{(0,r),P}^- \right)$, only then radar at (x, y) will be an element of Φ_k^I .

B. Interfering Distance

Our objective is to determine the impact of the interfering radars located on the ego radar's street and the remaining streets on the detection performance of the ego radar. To do so, we determine the fraction length of $L_i, \forall L_i \in \{\mathcal{P}_P, \mathcal{P}_B\}$ wherein if a radar is present, it will contribute to the interference experienced at the ego radar. First, note that the distance from the ego radar to the intersection of the L_i th line is

$$d_i = u_i - r_0 = \frac{r_i}{\sin \theta_i} - r_0, \quad (4)$$

where the angle of intersection is equal to the generating angle θ_i of the intersecting line and $r_0 = 0$ in the case of PLCP. The distance between the interfering radar on L_i from the intersection point is $v_{k,i}$, referred to as the interfering distance if the other radar and ego radar mutually interfere. Figure 4 illustrates an ego radar with a green radar sector on L_1 and radars mounted on other vehicles, S and T , on L_i , with red and purple beams. Specifically, S and T are at a distance $v_{k,i} = b_{k,i}$ and $v_{k,i} = a_{k,i}$ from the intersection point, respectively. These two distances ($a_{k,i}$ and $b_{k,i}$) represent the bounds of $v_{k,i}$ within which another radar will interfere with the ego radar. From Fig 4, any other vehicle present behind the vehicle S will not cause interference. Likewise, any vehicle present after vehicle T also will not cause interference. This is because the vehicles present behind S and after T will not mutually interfere with ego radar.

From definition 1, the radar sector of ego vehicle is bounded as the maximum range R_k to interferers is limited by either blockages or by the maximum detectable/unambiguous range of the radar. Thus, R_k must be considered to find the interfering distance. The following Theorem 1 gives the maximum and minimum interfering distance i.e., $a_{B,i}$ and $b_{B,i}$ for BLCP.

Theorem 1. For L_i line with parameters (θ_i, r_i) intersecting L_0 at a distance d_i from the ego radar, the maximum ($a_{B,i}$) and the minimum ($b_{B,i}$) distances of the interfering radars from the point of intersection on L_i , for BLCP are given as:

$$a_{B,i} =$$

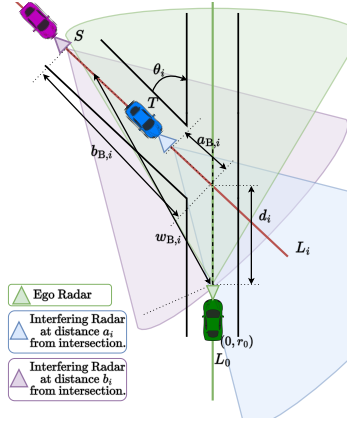


Fig. 4. Illustration of a scenario where two radars are present at the edge point of the line L_i inducing interference.

$$a_{P,i} = \begin{cases} R; & \text{for } (\theta_0, r_0) = (0, 0) \\ d_i (|\sin \theta_i| \cot \Omega - |\cos \theta_i|); & \text{for } 0 \leq d_i \leq c_2, \\ & \text{and } \theta_i \in [0, 2\pi] \setminus \{[\Omega, \pi - \Omega] \cup [\pi + \Omega, 2\pi - \Omega]\} \\ \frac{d_i |\sin(\theta_i - \Omega)|}{\sin \Omega}; & \text{for } 0 \leq d_i \leq c_2, \\ & \text{and } \theta_i \in \{[\Omega, 2\Omega] \cup [\pi + \Omega, \pi + 2\Omega]\} \\ \frac{d_i |\sin(\theta_i + \Omega)|}{\sin \Omega}; & \text{for } 0 \leq d_i \leq c_2, \\ & \text{and } \theta_i \in \{\pi - 2\Omega, \pi - \Omega\} \cup [2\pi - 2\Omega, 2\pi - \Omega] \\ \frac{d_i}{|\sin \theta_i| \cot \Omega - |\cos \theta_i|}; & \text{for } c_1 \leq d_i < 0, \\ & \text{and } \theta_i \in [0, 2\pi] \setminus \{[\Omega, \pi - \Omega] \cup [\pi + \Omega, 2\pi - \Omega]\} \\ 0; & \text{otherwise} \end{cases} \quad (5)$$

$$b_{P,i} = \begin{cases} R_B; & \text{for } (\theta_0, r_0) = (0, 0) \\ \sqrt{R_B^2 - (d_i \sin \theta_i)^2} - d_i |\cos \theta_i|; & \text{for } c_1 \leq d_i \leq c_2, \\ & \text{and } \theta_i \in [0, 2\pi] \setminus \{[2\Omega, \pi - 2\Omega] \cup [\pi + 2\Omega, 2\pi - 2\Omega]\} \\ \frac{d_i \tan \Omega}{|\sin \theta_i| - \tan \Omega |\cos \theta_i|}; & \text{for } 0 \leq d_i \leq c_1 \\ & \text{and } \theta_i \in \{[\Omega, 2\Omega] \cup [\pi - 2\Omega, \pi - \Omega]\} \\ 0; & \text{otherwise} \end{cases} \quad (6)$$

where,

$$c_1 = R_B \sin \Omega (\cot \Omega - |\cot \theta|), \quad c_2 = R_B |\csc \theta| \sin \Omega$$

Proof. See Appendix A for the complete proof. \square

For the PLCP model, the values of $a_{P,i}$ and $b_{P,i}$ are structurally same as $a_{B,i}$ and $b_{B,i}$, but the only difference lies in parameters d_i , R_P , and most importantly the cases for different angles of θ_i . For the PLCP, d_i reduces to u_i as $r_0 = 0$ from (4). In (5) and (6), the set of values of θ_i for all the different cases has a larger range as compared to different cases seen in Lemma 1. For example, $a_{B,i} = d_i (|\sin \theta_i| \cot \Omega - |\cos \theta_i|)$ if $\theta_i \in [0, 2\pi] \setminus \{[\Omega, \pi - \Omega] \cup [\pi + \Omega, 2\pi - \Omega]\}$, while as in Lemma 1, for the same scenario, the range of θ_i is $\{[0, \Omega] \cup [\pi - \Omega, \pi]\}$. Because of the non-homogeneous construction of BLP, we have to carefully consider all the different cases, which leads to a larger range of θ_i . As r_0 in BLP is dynamic thus, the values of $a_{B,i}$ and $b_{B,i}$ will exist

for such cases where the values of $a_{P,i}$ and $b_{P,i}$ do not exist.

Example: Consider the following example. In PLCP, the ego radar is at the origin, and if $\theta_i > \pi$, then line L_i does not intersect L_0 ahead of the ego radar, i.e., in $y > 0$. On the contrary, for the same range of generating angles, the location of ego radar can be such that line L_i can intersect the L_0 ahead of the ego radar. This complexity introduced by r_0 leads to a careful consideration of θ_i in determining the interfering distance in BLP in comparison to PLCP.

Lemma 1. For line L_i that intersects L_0 at a distance d_i from the ego radar, the maximum ($a_{P,i}$) and the minimum ($b_{P,i}$) distances of the interfering radars from the point of intersection on L_i , are given as:

$$a_{P,i} = \begin{cases} R; & \text{for } (\theta_0, r_0) = (0, 0) \\ u_i (|\sin \theta_i| \cot \Omega - |\cos \theta_i|); & \text{for } 0 \leq u_i \leq c_2, \\ & \text{and } \theta_i \in \{[0, \Omega] \cup [\pi - \Omega, \pi]\} \\ \frac{u_i |\sin(\theta_i - \Omega)|}{\sin \Omega}; & \text{for } 0 \leq u_i \leq c_2, \text{ and } \theta_i \in [\Omega, 2\Omega] \\ \frac{u_i |\sin(\theta_i + \Omega)|}{\sin \Omega}; & \text{for } 0 \leq u_i \leq c_2, \\ & \text{and } \theta_i \in [\pi - 2\Omega, \pi - \Omega] \\ \frac{u_i}{|\sin \theta_i| \cot \Omega - |\cos \theta_i|}; & \text{for } c_1 \leq u_i < 0 \\ & \text{and } \theta_i \in \{[\pi, \pi + \Omega], [2\pi - \Omega, 2\pi]\} \\ 0; & \text{otherwise} \end{cases} \quad (7)$$

$$b_{P,i} = \begin{cases} R_P; & \text{for } (\theta_0, r_0) = (0, 0) \\ \sqrt{R_P^2 - (u_i \sin \theta_i)^2} - u_i |\cos \theta_i|; & \text{for } c_1 \leq u_i \leq c_2, \\ & \text{and } \theta_i \in \{[0, \Omega] \cup [\pi - \Omega, \pi + \Omega] \cup [2\pi - \Omega, 2\pi]\} \\ \frac{u_i \tan \Omega}{|\sin \theta_i| - \tan \Omega |\cos \theta_i|}; & \text{for } 0 \leq u_i \leq c_1 \\ & \text{and } \theta_i \in \{[\Omega, 2\Omega] \cup [\pi - 2\Omega, \pi - \Omega]\} \\ 0; & \text{otherwise} \end{cases} \quad (8)$$

where,

$$c_1 = R_P \sin \Omega (\cot \Omega - |\cot \theta|), \quad c_2 = R_P |\csc \theta| \sin \Omega$$

With all the possible cases where we derived the interfering distance, i.e., $v_{k,i}$, correspondingly, the distance from the ego radar to the interfering radar is then given as

$$w_{k,i} = \begin{cases} v_{k,i} & i = 0 \\ \sqrt{(d_i + v_{k,i} |\cos \theta_i|)^2 + (v_{k,i} \sin \theta_i)^2} & \text{otherwise.} \end{cases} \quad (9)$$

Leveraging the results from Theorem 1 and Lemma 1, we determine the average number of interferers experienced by the ego radar based on its location. To determine the average number of interferers, we first estimate the average length of the fraction of a single line L_i , which falls within the radar sector. We average out the maximum and minimum of $v_{k,i}$, i.e., $b_{k,i}$ and $a_{k,i}$ respectively, to find the average length of a single interfering line. Following this, we compute the average number of interferers \mathcal{I}_k , by taking the product of the average

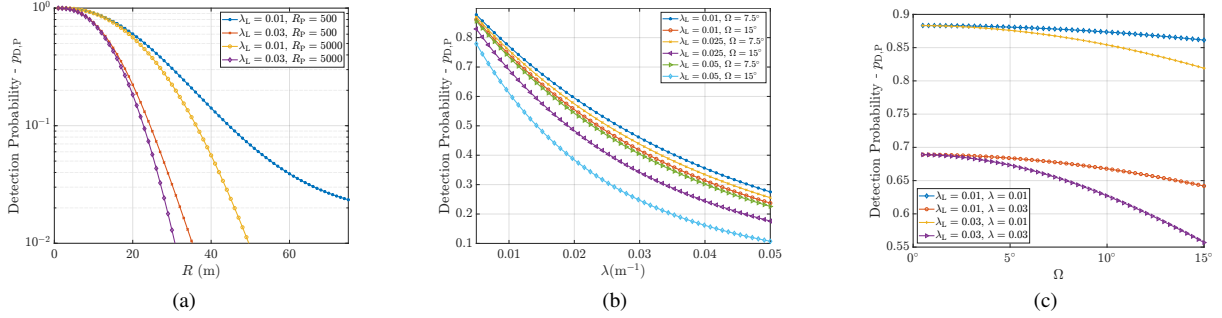


Fig. 5. Probability of successful detection $p_{D,P}$ with respect to (a) R , (b) λ , and (c) Ω .

length of all lines with λ . As an example, for the BLCP case, the derived values of $b_{k,i}$ and $a_{k,i}$ given in (5) and (6) is used to compute \mathcal{I}_B as,

$$\mathcal{I}_B(r_0) = \lambda \left(\frac{1}{2\pi R_B} \int_0^{R_B} \int_0^{2\pi} |b_B - a_B| d\theta dr \right)^{n_B}. \quad (10)$$

IV. DETECTION SUCCESS PROBABILITY

The detection *success probability* at a threshold β is defined as the complementary cumulative density function (CCDF) of SIR, $p_{D,P}(\beta) = \mathbb{P}[\text{SIR} > \beta]$. This represents the probability that an attempted detection by the ego radar of the target located at a distance R is successful. We derive the detection success probability for both PLCP and BLCP modeled networks and draw insights from them in conjunction with real-world road and traffic parameters.

Theorem 2. For the network where locations of the vehicles are modeled as Cox process Φ_k , such that $k \in \{P, B\}$ the detection success probability for an ego radar is

$$p_{D,k}(\beta) = \mathbb{E}_{\mathcal{D}_k} \left(\prod_{(\theta,r) \in \mathcal{D}_k} \mathbb{E}_{\Phi} \left(\prod_{\mathbf{w}_k \in \Phi_{k_0}} \frac{1}{1 + \beta' \|\mathbf{w}_k\|^{-\alpha}} \right) \right) \quad (11)$$

where $\beta' = \frac{4\pi\beta}{\bar{\sigma}R^{-2\alpha}}$, and $\|\mathbf{w}_k\|$ is given in (9).

Proof. From the definition of success probability, we have

$$\begin{aligned} p_{D,k}(\beta) &= \mathbb{P} \left(\frac{\gamma\sigma_c P R^{-2\alpha}}{\sum_{\mathbf{w}_k \in \Phi_{k_0}} 4\pi\gamma P h_{\mathbf{w}_k} \|\mathbf{w}_k\|^{-\alpha}} > \beta \right) \\ &= \mathbb{P} \left(\sigma_c > \frac{\beta \left(\sum_{\mathbf{w}_k \in \Phi_{k_0}} 4\pi\gamma P h_{\mathbf{w}_k} \|\mathbf{w}_k\|^{-\alpha} \right)}{\gamma P R^{-2\alpha}} \right) \\ &\stackrel{(a)}{=} \mathbb{E}_{\Phi_{k_0}, h_{\mathbf{w}_k}} \left[\exp \left(- \frac{\beta \left(\sum_{\mathbf{w}_k \in \Phi_{k_0}} 4\pi\gamma P h_{\mathbf{w}_k} \|\mathbf{w}_k\|^{-\alpha} \right)}{\bar{\sigma} \gamma P R^{-2\alpha}} \right) \right] \\ &= \mathbb{E}_{\mathcal{D}_k \cup (0,0)} \left(\prod_{(\theta,r) \in \{\mathcal{D}_k \cup (0,0)\}} \mathbb{E}_{\Phi} \left(\prod_{\mathbf{w}_k \in \Phi} \mathbb{E}_{h_{\mathbf{w}_k}} \left[\exp \left(- \frac{4\pi\beta P h_{\mathbf{w}_k} \|\mathbf{w}_k\|^{-\alpha}}{\bar{\sigma} P R^{-2\alpha}} \right) \right] \right) \right) \end{aligned}$$

$$\stackrel{(b)}{=} \mathbb{E}_{\mathcal{D}_k \cup (0,0)} \left(\prod_{(\theta,r) \in \{\mathcal{D}_k \cup (0,0)\}} \mathbb{E}_{\Phi} \left(\prod_{\mathbf{w}_k \in \Phi} \frac{1}{1 + \beta' \|\mathbf{w}_k\|^{-\alpha}} \right) \right) \quad (12)$$

Step (a) follows from the exponential distribution of σ_c . Step (b) follows by taking the average over fading $h_{\mathbf{w}_k}$. \square

Corollary 1. For $k = P$, i.e., the network is modeled by PLCP, the detection success probability $p_{D,P}(\beta)$ is given as,

$$p_{D,P}(\beta) = \exp \left(- \lambda \int_R^{R_P} 1 - \frac{1}{1 + \beta' v_P^{-\alpha}} dv_P - \lambda_L \int_{\mathbb{R}^+} \int_0^{2\pi} 1 - \exp \left(- \lambda \int_{a_P}^{b_P} 1 - \frac{1}{1 + \beta' \|\mathbf{w}_P\|^{-\alpha}} dv_P \right) d\theta dr \right). \quad (13)$$

Proof. The corollary follows by applying Laplace functional [31] of palm PLCP to (12). \square

Corollary 2. For $k = B$, i.e., the network is modeled by BLCP, the detection success probability $p_{D,B}(r_0, \beta)$ is given as,

$$p_{D,B}(r_0, \beta) = \exp \left(- \lambda \int_R^{R_B} 1 - \frac{1}{1 + \beta' v_B^{-\alpha}} dv_B \right) \times \left[\frac{1}{2\pi R_g} \int_0^{R_g} \int_0^{2\pi} \exp \left(- \lambda \int_{a_B}^{b_B} 1 - \frac{1}{1 + \beta' \|\mathbf{w}_B\|^{-\alpha}} dv_B \right) d\theta dr \right]^{n_B}. \quad (14)$$

We see that the detection success probability of BLCP $p_{D,B}(r_0, \beta)$ is a function of r_0 . This is because \mathbf{w}_B and limits of integration depend on ego radar's location, unlike PLCP. In the next section, we will see the performance analysis of detection probability, $p_{D,k}(\beta)$ for varying values of beamwidth, range, and intensity of vehicles.

V. NUMERICAL RESULTS AND DISCUSSION

This section highlights the results from a typical automotive radar PLCP and BLCP framework. The radar parameters used for the numerical results are taken from [34]. Specifically, $P = 10$ dBm, $\bar{\sigma} = 30$ dBsm, $\alpha = 2$, $G_t = G_r = 10$ dBi, $f_c = 76.5$ GHz, $N_d = -174$ dBm/Hz, $W = 25$ KHz, and $\beta = 10$ dB. We study how the success probability $p_{D,k}$ varies with system parameters like R , Ω , and λ . In all the plots, we assume $\Omega = 7.5^\circ$ (for PLCP models), $\Omega = 15^\circ$ (for BLCP models), $R = 15$ m, $\lambda = 0.01 \text{ m}^{-1}$, $R_g = 1500$ m, $n_B = 300$, and $R_k = 500$ m unless specified otherwise.

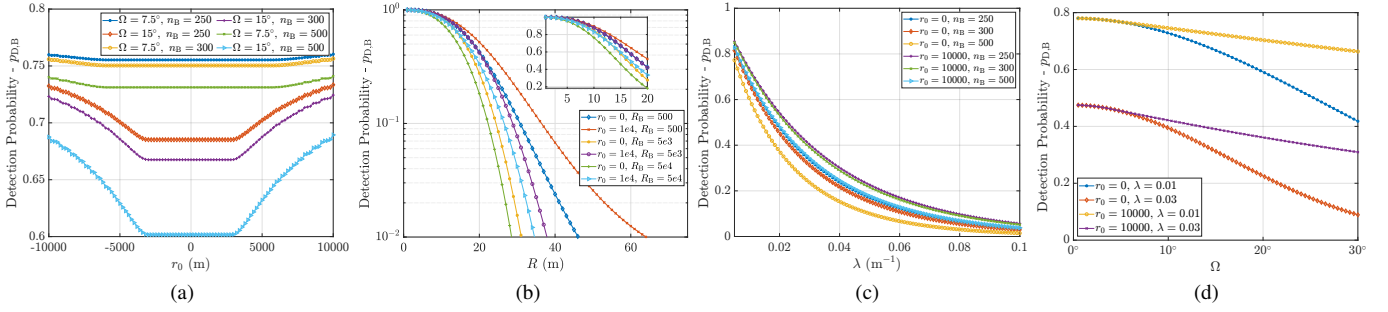


Fig. 6. Probability of successful detection $p_{D,B}$ with respect to (a) r_0 , (b) R , (c) λ , and (d) Ω .

A. Success Probability

1) *PLCP*: We first plot $p_{D,P}$ with respect to R , i.e., the range in Fig 5a. The probability of successful detection decreases as R increases due to increased path loss. This trend is observed irrespective of the value of beamwidth, λ_L , and λ . Furthermore, the $p_{D,P}$ is higher when the interference from neighboring radars is lower due to a low vehicle density. Next, we examine the variation of success probability with λ in Fig 5b. The results indicate that $p_{D,P}$ decreases with λ due to an increase in the total number of interferers and a decrease of the distance between the nearest interfering radar and the ego radar at the origin. For a fixed beamwidth, $p_{D,P}$ decreases as λ_L increases. Similar trends is observed between $p_{D,P}$ and radar beamwidth in Fig. 5c. We note that intensity has a greater impact on total interference than beamwidth.

Fig. 5c shows that as the beamwidth increases the number of interfering radars within the main lobe of the ego radar increases, thereby decreasing the detection probability. For lower Ω (e.g., $< 5^\circ$) and given λ , the impact of λ_L is limited, since, in case of small beamwidths, the number of interferers present on the remaining lines of PLP are negligible as compared to interferes present on ego radars street, i.e., L_0 .

2) *BLCP*: Unlike the detection performance of ego radar in the PLCP framework, the BLCP scenario presents a contrasting view of detection probability $p_{D,B}$ against different parameters. Fig. 6a shows that as the ego radar moves from the outskirts of a city ($r_0 = -10000$ m) to its center ($r_0 = 0$ m), then back to the outskirts ($r_0 = +10000$ m), the detection probability first decreases, then saturates to a certain level and subsequently increases as the vehicle leaves the city. Recall that the axis vector of the ego radar is $\mathbf{a} = (0, 1)$. Although the street geometry is isotropic, the radar sector is not. Consequently, the detection performance at -10000 m is not the same as that at 10000 m. The ego radar at -10000 m has lower $p_{D,B}$ as compared to 10000 m. This is because, at $r_0 = -10000$ m, the radar sector of ego radar has a higher number of interfering radars falling inside it than at $r_0 = 10000$ m. We further observe that for smaller values of beamwidth, we have a larger saturation region as compared to larger values of Ω . We have assumed $R_g = 1500$ m and $R_B = 500$ m. Thus the detection probability for the ego radar in the BLCP model **should have been constant** from $r_0 = -1500$ m to $r_0 = 500$ m m irrespective of of Ω . However, this is not the case. From Theorem 2 of [32], we deduce that the *line length density* is constant in the

following range of values of $r_0 = [-1500, 500]$ m, as the radar sector is completely within the generating circle $\mathcal{C}((0, 0), R_g)$. This unusual behavior of the network performance where the saturation range of $p_{D,B}$ is not equal to $r_0 = [-1500, 500]$ m will be explained in the subsection V-B.

In Figure. 6b we plot $p_{D,B}$ versus the distance to target, R . As R increases, the detection performance deteriorates since the target-scattered signal decreases due to the two-way path loss, while the interference power remains the same. Likewise, by increasing R_B from 500 m to 50000 m, $p_{D,B}$ decreases, as the total number of interferers within the radar sector increases. Now, in Figure. 6c, we plot the detection probability with respect to the intensity of vehicles, λ , for two different locations of the ego radar. As evident from the plot, $p_{D,B}$ decreases as λ increases due to an increase in interference. Additionally, we observe that, for $r_0 = \pm 10000$ m (outskirts), $p_{D,B}$ is at a larger value than for $r_0 = 0$ (city center). This is because the line length/street density at the outskirts is lower than at the city center. Also, as n_B increases from 250 to 500 , we observe that, for a constant value of λ , the detection probability decreases because a higher number of streets result in a larger number of vehicles.

Finally we plot $p_{D,B}$ w.r.t. half-power beamwidth Ω for different values of r_0 and λ . As Ω increases from 1° to 15° , the detection probability decreases non-linearly. We observe that at the city center, the impact of Ω on the detection performance is more significant as compared to $r_0 = 10000$. Furthermore, for a given value of λ , the detection probability for initial values of Ω is nearly the same for two values of $r_0 = \{0, 10000\}$. Indeed, similar to the PLCP, for low beamwidth values, the street containing the ego radar contributes more significantly to the interference as compared to the other streets. In subsection V-C, we compare the performance of BLCP and PLCP frameworks to better understand the contrasting results of these two radar frameworks.

B. Average number of interferers

In this subsection, we explain the phenomenon when the detection probability remains constant for a specific range of r_0 . Figure 7a plots \mathcal{I}_B given in (10) w.r.t. the location of ego radar for the same values of Ω and n_B as in Fig. 6a. We see that \mathcal{I}_B first increases as r_0 increases from -10000 m, then saturates at a value and decreases again. The region where it starts to saturate and then again decreases corresponds to the same range of values, for which $p_{D,B}$ remains constant

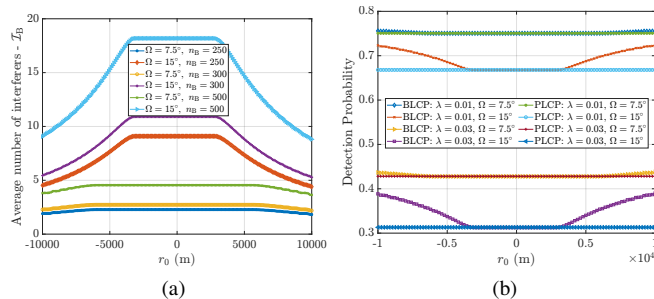


Fig. 7. (a) Average number of interferers falling inside the bounded radar sector w.r.t r_0 . (b) Comparison of $p_{D,k}$ of ego radar for PLCP and BLCP models w.r.t r_0 .

in Fig. 6a. Accordingly, the saturation range is not equal to $[-1500, 500]$ m. Rather, the saturation range is a function of Ω , R_B and R_g , and not the function of n_B and λ . In Fig. 7a and Fig. 6a, the region of saturation remains the same i.e. $r_0 = -3100$ m to $r_0 = 2800$ m for $\Omega = 7.5^\circ$ and $n_B = \{250, 300, 500\}$. Likewise, the region of saturation is from $r_0 = -6000$ m to $r_0 = 5700$ m in both Fig. 7a and Fig. 6a for $\Omega = 7.5^\circ$ and $n_B = \{250, 300, 500\}$.

Example: Let the ego radar be present at the origin with axis vector $\mathbf{a} = (0, 1)$, and let $\Omega < 1^\circ$, i.e., negligible. Here, the detection probability performance does not change as the ego radar moves anywhere in the city, and it depends only on the intensity of vehicles present on line L_0 since the beamwidth is too narrow to be impacted by cars on other lanes. Thus, we expect a constant $p_{D,B}$. As the beamwidth increases, the ego radar incorporates more interfering radars. For $\Omega = 2\pi$ corresponding to an isotropic radar sector, we see the saturation region equal $[-1500, 500]$ m.

C. Detection performance of BLCP v/s PLCP

Figure 7b compares the detection probability $p_{D,k}$ for both the PLCP and BLCP based model networks. To make a fair comparison, we take the intensity of lines of PLP as $\lambda_L = \frac{300}{2\pi \cdot 1500}$ and number of lines in BLP $n_B = 300$. The detection probability presents a broad contrast between the PLCP and BLCP networks. In the PLCP model, there are no insights on the detection probability depending on the location of ego radar. Due to the homogeneous nature of the PLCP the $p_{D,P}$ remains constant at all value of r_0 . On the other hand, BLCP highlights the impact of the ego radar location. Interestingly, we observe that the detection probability for the PLCP model are the same as for the BLCP in the saturation region, especially if the generating circle is large. The PLCP can be used to model the network instance of a local section of the city with a homogeneous distribution of lanes, while the BLCP can model the road structure of an entire city, and the two models can be used to study the performance of an ego radar on a micro or macro scale. The following section introduces a real-world perspective of modeling road networks using PLCP and BLCP framework, where we learn of how PLCP and BLCP can be used in modeling different perspectives of the city network.

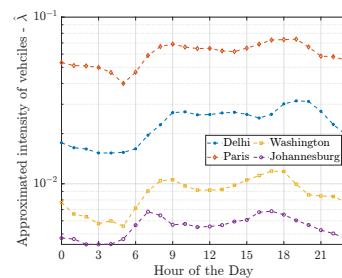


Fig. 8. $\hat{\lambda}$ w.r.t. hour of the day for four cities

D. Performance of ego radar in real-world road geometries

This section analyzes the urban traffic patterns by generating detailed geospatial maps for four major metropolitan areas: New Delhi, Paris, Washington, and Johannesburg. These maps include detailed road networks and important urban infrastructure. They also extend to surrounding areas, comprehensively illustrating the urban sprawl and its effects on traffic patterns. To generate the road networks, we use the OSMnx Python module that models, analyzes, and visualizes OpenStreetMap street networks [35]. Using this real-world data, we approximate the parameters for the PLP and BLP, enabling a robust statistical representation of road patterns. In Table II, the first column illustrates the road network of the four major cities, and in the second column, we extend the maps to cover the greater suburban areas corresponding to each of the cities. The data of the road networks shown in the first column is used to approximate the PLCP parameter λ_L . For PLP, the total length of lines in a given region is the product of the λ_L and the region's area. By considering the geographical region to be a circle, we estimate the approximate street/line density, $\hat{\lambda}_L$, as the street density of each city obtained from the OSMnx package divided by π . The $\hat{\lambda}_L$ for the four cities are $\{0.004, 0.0052, 0.0053, 0.0037\} \text{ m}^{-1}$. Now, to fit the BLP model, we use the *total length of street* obtained from OSMnx data and the result of Theorem 2 from [32]. This Theorem derives the *line length density* $\rho(r)$ of BLP, where r is the distance from the center of the generating circle. The Theorem shows that $\rho(r)$ first remains constant up to R_g , and then decreases as $\mathcal{O}(r)$, as $r \rightarrow \infty$. By integrating $\rho(r)$ over the region of interest, we get the area's total length of BLP lines. In our analysis, we assume that at the center of each city, there is a square bounding box of a specific length, and we calculate the total length of lines as the dimensions of the box increase. The third column of Table II plots the total length of lines w.r.t the dimensions of the box. Using this data, we curve fit parameters n_B and R_g using the equations of Theorem 2 [32] integrated over the area of the bounding box. As an example in the third column and first row, the approximated parameters for Delhi, India are $\hat{n}_B = 662$ and $\hat{R}_g = 12.96$ Km. Likewise, in the second column, approximated parameters \hat{n}_B and \hat{R}_g for other cities can be found. In the third column, we see how well the approximated parameters fit w.r.t real-world data. These plots exhibit remarkable precision in modeling road networks, especially in the varied and intricate urban settings of Delhi, Paris, Washington, and Johannesburg. The empirical investigation demonstrates a strong correlation between the BLCP models and real road structures.

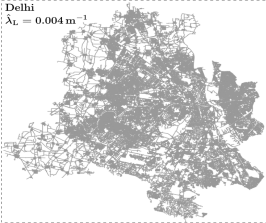

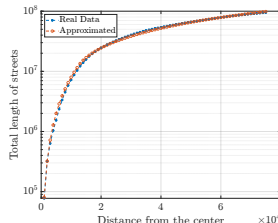
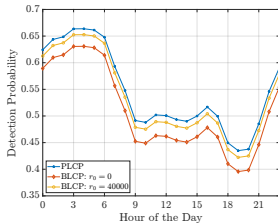
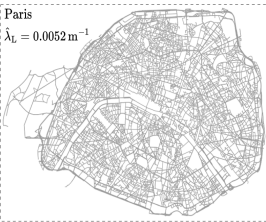
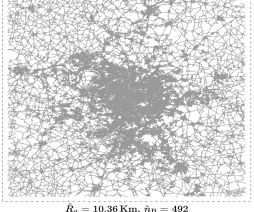
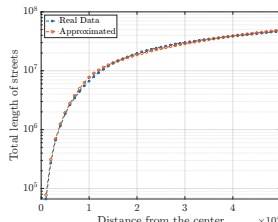
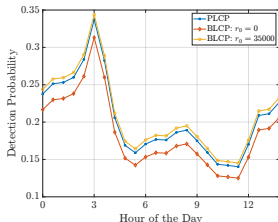
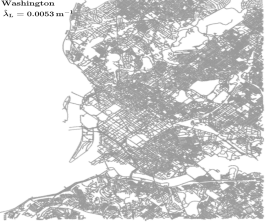
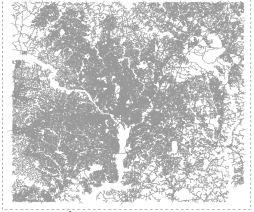
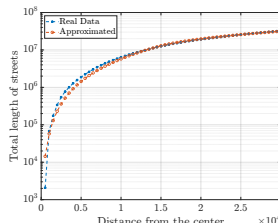
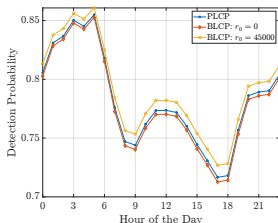


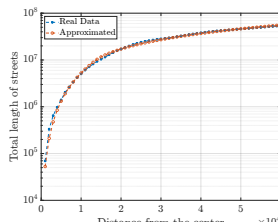
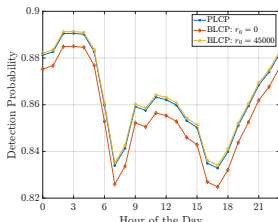
Map of Cities considered for PLCP	Extended Map of Cities considered for BLCP	Fitting BLCP parameters (n_B, R_g) to real data	Detection performance of PLCP and BLCP
 <p>Delhi $\lambda_L = 0.004 \text{ m}^{-1}$</p>	 <p>$R_g = 12.96 \text{ Km}, \hat{n}_B = 662$</p>		
 <p>Paris $\lambda_L = 0.0052 \text{ m}^{-1}$</p>	 <p>$R_g = 10.36 \text{ Km}, \hat{n}_B = 492$</p>		
 <p>Washington $\lambda_L = 0.0063 \text{ m}^{-1}$</p>	 <p>$R_g = 15.16 \text{ Km}, \hat{n}_B = 550$</p>		
 <p>Johannesburg $\lambda_L = 0.0037 \text{ m}^{-1}$</p>	 <p>$R_g = 14.08 \text{ Km}, \hat{n}_B = 470$</p>		

Table II: City maps and their corresponding detection performance across the hour of the day

Finally, we consider the vehicular density on the roads. This parameter is a function of the nature of a city - cities with extensive public transport generally have fewer vehicles - as well as the time of the day - peak hours have higher vehicular density than off-peak hours. Therefore, in the fourth column of Table II, we plot the detection probability of an ego radar for the four cities modeled using the approximated parameters w.r.t to the hour of the day. To do so, we compute the vehicular density, i.e., λ at each hour from the report in [36]. The traffic density, or the hourly average number of vehicles, tends to have a bimodal profile with morning and evening peaks. In addition, we utilize the hourly congestion C_i data provided by TomTom [37] to factor the hourly fluctuations in congestion. From this data, we determine the hour of the day when the congestion is at its peak and then compute the average number of vehicles at this hour. Figure 12 of [36] showcases the percent of average daily traffic w.r.t hour of the day, where the peak traffic occupancy percentage is around 8%. By taking the product of peak traffic occupancy percentage and total number of non-commercial vehicles present in the city and then dividing it by the total length of roads, it gives the approximated $\hat{\lambda}_{\max}$ at peak congestion hour. Assuming a linear relation between the intensity of vehicles and the congestion

percentage, we approximate the λ for all other hours employing the data from TomTom, using $\hat{\lambda}_i = \hat{\lambda}_{\max} C_i / C_{\max}$, where $\hat{\lambda}_i$ is the vehicular intensity, C_i is the congestion percentage at i^{th} hour, and C_{\max} is the maximum congestion percentage. Figure. 8 illustrates λ w.r.t hour of the day for the four cities. Here, Paris has a higher intensity of vehicles across all hours than the other three cities. In the fourth column, we plot the corresponding detection probability of an ego radar for both PLCP and BLCP frameworks with r_0 at the city center and city outskirts w.r.t to the hour of the day. As anticipated, the overall detection probability is the poorest in Paris, which has high traffic intensity, followed by Delhi, and Washington, while Johannesburg performs best. These results are consistent with the traffic index ranking provided by TomTom. In each city, the radars perform best in the early morning hours between 3 and 5 am when vehicular traffic is at its lowest.

VI. CONCLUSION

This research paper has presented a comprehensive analysis of large-scale automotive radar networks, considering the impact of street geometry and vehicular density. By employing SG-based models, we account for homogeneous and inhomogeneous street distributions using PLCP and BLCP models

respectively, providing a complete understanding of radar performance in different urban contexts. Our models bridge simplistic, highway-based assumptions and the complexity of real urban environments and provide crucial insights into radar interference mitigation in dense city centers and suburbs. By deriving the effective interference set and characterizing the detection probability of an ego radar, we demonstrated how radar performance can be significantly influenced by urban street layouts and traffic conditions. The PLCP model excels at dense urban regions, while the BLCP model captures the city center-to-outskirts transition. The validation of our models with real-world data further strengthens their applicability in urban radar network planning. This research helps automotive manufacturers and network operators optimize radar systems for urban layouts and traffic conditions, improving advanced driver assistance system safety and efficiency. Network operators can utilize these models to evaluate the number of successful detection and then utilize this parameter to optimize beamwidth. This framework can be expanded to include dynamic traffic models and study how urban infrastructure changes radar network performance.

REFERENCES

- [1] N. Lu, N. Cheng, N. Zhang, X. Shen, and J. W. Mark, "Connected vehicles: Solutions and challenges," *IEEE internet of things journal*, vol. 1, no. 4, pp. 289–299, 2014.
- [2] I. Bilik, O. Longman, S. Villeval, and J. Tabrikian, "The rise of radar for autonomous vehicles: Signal processing solutions and future research directions," *IEEE signal processing Magazine*, vol. 36, no. 5, pp. 20–31, 2019.
- [3] D. M. Grimes and T. O. Jones, "Automotive radar: A brief review," *Proceedings of the IEEE*, vol. 62, no. 6, pp. 804–822, 1974.
- [4] H. Hartenstein and L. Laberteaux, "A tutorial survey on vehicular ad hoc networks," *IEEE Communications magazine*, vol. 46, no. 6, pp. 164–171, 2008.
- [5] H. H. Meinel and J. Dickmann, "Automotive radar: From its origins to future directions," *Microwave Journal*, vol. 56, no. 9, 2013.
- [6] C. Waldschmidt, J. Hasch, and W. Menzel, "Automotive radar—from first efforts to future systems," *IEEE Journal of Microwaves*, vol. 1, no. 1, pp. 135–148, 2021.
- [7] M. Goppelt, H.-L. Blöcher, and W. Menzel, "Automotive radar—investigation of mutual interference mechanisms," *Advances in Radio Science*, vol. 8, pp. 55–60, 2010.
- [8] S. Alland, W. Stark, M. Ali, and M. Hegde, "Interference in automotive radar systems: Characteristics, mitigation techniques, and current and future research," *IEEE Signal Processing Magazine*, vol. 36, no. 5, pp. 45–59, 2019.
- [9] A. Al-Hourani, R. J. Evans, S. Kandeepan, B. Moran, and H. Eltom, "Stochastic geometry methods for modeling automotive radar interference," *IEEE Transactions on Intelligent Transportation Systems*, vol. 19, no. 2, pp. 333–344, 2017.
- [10] G. Ghatak, S. S. Kalamkar, and Y. Gupta, "Radar detection in vehicular networks: Fine-grained analysis and optimal channel access," *IEEE Transactions on Vehicular Technology*, vol. 71, no. 6, pp. 6671–6681, 2022.
- [11] G. M. Brooker, "Mutual interference of millimeter-wave radar systems," *IEEE Transactions on Electromagnetic Compatibility*, vol. 49, no. 1, pp. 170–181, 2007.
- [12] M. Goppelt, H.-L. Blöcher, and W. Menzel, "Analytical investigation of mutual interference between automotive fmcw radar sensors," in *2011 German Microwave Conference*, pp. 1–4, IEEE, 2011.
- [13] T. Schipper, S. Prophet, M. Harter, L. Zwirello, and T. Zwick, "Simulative prediction of the interference potential between radars in common road scenarios," *IEEE Transactions on Electromagnetic Compatibility*, vol. 57, no. 3, pp. 322–328, 2015.
- [14] A. Munari, L. Simić, and M. Petrova, "Stochastic geometry interference analysis of radar network performance," *IEEE Communications Letters*, vol. 22, no. 11, pp. 2362–2365, 2018.
- [15] P. Chu, J. A. Zhang, X. Wang, Z. Fei, G. Fang, and D. Wang, "Interference characterization and power optimization for automotive radar with directional antenna," *IEEE Transactions on Vehicular Technology*, vol. 69, no. 4, pp. 3703–3716, 2020.
- [16] Z. Fang, Z. Wei, X. Chen, H. Wu, and Z. Feng, "Stochastic geometry for automotive radar interference with rcs characteristics," *IEEE Wireless Communications Letters*, vol. 9, no. 11, pp. 1817–1820, 2020.
- [17] K. V. Mishra, B. S. MR, and B. Ottersten, "Stochastic-geometry-based interference modeling in automotive radars using matern hard-core process," in *2020 IEEE Radar Conference (RadarConf20)*, pp. 1–5, IEEE, 2020.
- [18] L. Kui, S. Huang, and Z. Feng, "Interference analysis for automotive radar using matern hard-core point process," in *2021 IEEE/CIC International Conference on Communications in China (ICCC)*, pp. 817–822, IEEE, 2021.
- [19] J. Huang, Z. Fei, T. Wang, X. Wang, F. Liu, H. Zhou, J. A. Zhang, and G. Wei, "V2x-communication assisted interference minimization for automotive radars," *China Communications*, vol. 16, no. 10, pp. 100–111, 2019.
- [20] M. Zhang, S. He, C. Yang, J. Chen, and J. Zhang, "Vanet-assisted interference mitigation for millimeter-wave automotive radar sensors," *IEEE Network*, vol. 34, no. 2, pp. 238–245, 2020.
- [21] C. Aydogdu, M. F. Keskin, N. Garcia, H. Wymeersch, and D. W. Bliss, "Radchat: Spectrum sharing for automotive radar interference mitigation," *IEEE Transactions on Intelligent Transportation Systems*, vol. 22, no. 1, pp. 416–429, 2019.
- [22] Y. Wang, Q. Zhang, Z. Wei, L. Kui, F. Liu, and Z. Feng, "Performance analysis of uncoordinated interference mitigation for automotive radar," *IEEE Transactions on Vehicular Technology*, 2023.
- [23] S. S. Ram, G. Singh, and G. Ghatak, "Estimating radar detection coverage probability of targets in a cluttered environment using stochastic geometry," in *2020 IEEE International Radar Conference (RADAR)*, pp. 665–670, IEEE, 2020.
- [24] S. S. Ram, G. Singh, and G. Ghatak, "Optimization of radar parameters for maximum detection probability under generalized discrete clutter conditions using stochastic geometry," *IEEE Open Journal of Signal Processing*, vol. 2, pp. 571–585, 2021.
- [25] S. S. Ram and G. Ghatak, "Estimation of bistatic radar detection performance under discrete clutter conditions using stochastic geometry," in *IEEE Radar Conference 2022*, 2022.
- [26] S. S. Ram, S. Singhal, and G. Ghatak, "Optimization of network throughput of joint radar communication system using stochastic geometry," *Frontiers in Signal Processing*, vol. 2, p. 835743, 2022.
- [27] S. Singhal, S. K. Biswas, and S. S. Ram, "Leo/meo-based multi-static passive radar detection performance analysis using stochastic geometry," in *2023 IEEE Radar Conference (RadarConf23)*, pp. 1–6, IEEE, 2023.
- [28] V. V. Chetlur and H. S. Dhillon, "Coverage and rate analysis of downlink cellular vehicle-to-everything (c-v2x) communication," *IEEE Transactions on Wireless Communications*, vol. 19, no. 3, pp. 1738–1753, 2019.
- [29] J. P. Jeyaraj, M. Haenggi, A. H. Sakr, and H. Lu, "The transdimensional poisson process for vehicular network analysis," *IEEE Transactions on Wireless Communications*, vol. 20, no. 12, pp. 8023–8038, 2021.
- [30] C.-S. Choi and F. Baccelli, "Los coverage area in vehicular networks with cox-distributed roadside units and relays," *IEEE Transactions on Vehicular Technology*, vol. 72, no. 6, pp. 7772–7782, 2023.
- [31] H. S. Dhillon and V. V. Chetlur, *Poisson line Cox process: Foundations and applications to vehicular networks*. Springer, 2020.
- [32] M. T. Shah, G. Ghatak, S. Sanyal, and M. Haenggi, "Binomial line cox processes: Statistical characterization and applications in wireless network analysis," *IEEE Transactions on Wireless Communications*, 2024.
- [33] D. Shnidman, "Expanded swerling target models," *IEEE Transactions on Aerospace and Electronic Systems*, vol. 39, no. 3, pp. 1059–1069, 2003.
- [34] M. Series, "Systems characteristics of automotive radars operating in the frequency band 76–81 ghz for intelligent transport. systems applications," *Recommendation ITU-R, M*, pp. 2057–1, 2014.
- [35] G. Boeing, "Modeling and analyzing urban networks and amenities with osmnx," 2024.
- [36] M. E. Hallenbeck, M. Rice, B. Smith, C. Cornell-Martinez, J. Wilkinson, et al., "Vehicle volume distributions by classifications," tech. rep., United States. Federal Highway Administration, 1997.
- [37] TomTom, "Maps and location technology," <https://www.tomtom.com/>, 2024.

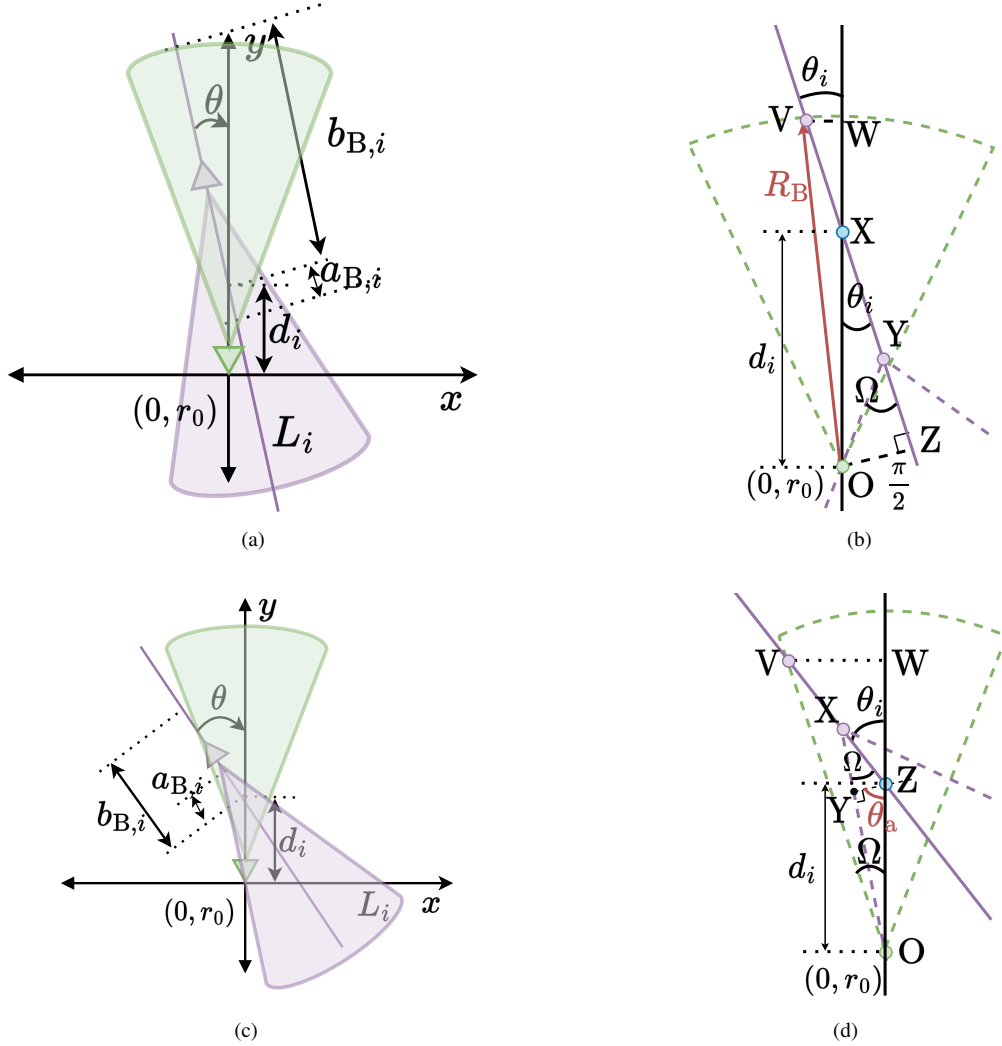


Fig. 9. (a) and (b) *Subcase (a)* of Case 1, and (c) and (d) *Subcase (b)* of Case 1 with generating angle present in the first quadrant in all four figures.

APPENDIX A PROOF OF THEOREM 1

Proof. We carefully consider all possible scenarios in which the ego radar is experiencing interference and then derive the distance to the interfering radars. To calculate the interfering distance, we apply basic trigonometric manipulations and examine all intersecting distance d_i and angle of intersection θ_i values. The value of d_i is calculated from the perspective of r_0 , and it can be positive or negative depending on the boresight direction \mathbf{a} . Suppose the ego radar is at origin i.e. $r_0 = 0$ and $\mathbf{a} = (-1, 0)$. If L_i intersects L_0 such that the point of intersection falls within the radar sector, we say that the intersection is taking place ahead of the ego radar, thus $d_i \geq 0$. If the intersection occurs outside the radar sector with the point of intersection on the negative y-axis, we say that intersection is taking place behind the ego radar therefore $d_i < 0$. Thus depending on the values of θ_i , r_i , r_0 , and Ω , we see that (5) and (6) consists of three major cases. First when the intersection is happening ahead of ego radar, but within R_B , i.e., $0 \leq d_i \leq R_B$, second when $d_i > R_B$. The third case is when the intersection is happening behind the ego radar, i.e., $d_i < 0$. To better explain the proof, we have divided it into

three parts of 3 major scenarios. Before we derive interfering distance for the said three cases, we introduce eight events depending on the value of θ_i , which are as

$$A_i = \begin{cases} A_1 = \{\theta_i : 0 \leq \theta_i \leq \Omega \text{ and } 0 \leq \theta_i \leq \frac{\pi}{2}\} \\ A_2 = \{\theta_i : \Omega < \theta_i \leq 2\Omega \text{ and } 0 \leq \theta_i \leq \frac{\pi}{2}\} \\ A_3 = \{\theta_i : \Omega \leq \pi - \theta_i \leq 2\Omega \text{ and } \frac{\pi}{2} < \theta_i \leq \pi\} \\ A_4 = \{\theta_i : 0 \leq \pi - \theta_i < \Omega \text{ and } \frac{\pi}{2} < \theta_i \leq \pi\} \\ A_5 = \{\theta_i : 0 \leq \theta_i - \pi \leq \Omega \text{ and } \pi < \theta_i \leq \frac{3\pi}{2}\} \\ A_6 = \{\theta_i : \Omega < \theta_i - \pi \leq 2\Omega \text{ and } \pi < \theta_i \leq \frac{3\pi}{2}\} \\ A_7 = \{\theta_i : \Omega \leq 2\pi - \theta_i \leq 2\Omega \text{ and } \frac{3\pi}{2} < \theta_i \leq 2\pi\} \\ A_8 = \{\theta_i : 0 \leq 2\pi - \theta_i < \Omega \text{ and } \frac{3\pi}{2} < \theta_i \leq 2\pi\}. \end{cases} \quad (15)$$

Let Θ be the union of events A_i i.e. $\Theta = \cup_i A_i$. Thus Θ is the set of θ_i wherein if an automotive radar is present on L_i may have an odds to has cause interference to ego radar. It further depends on r_i and r_0 whether the radars present on L_i can cause interference. The first two events of (15), i.e., $[A_1 \cup A_2]$ corresponds to the scenario when generating angle is in the first quadrant, likewise event $[A_3 \cup A_4]$, $[A_5 \cup A_6]$,

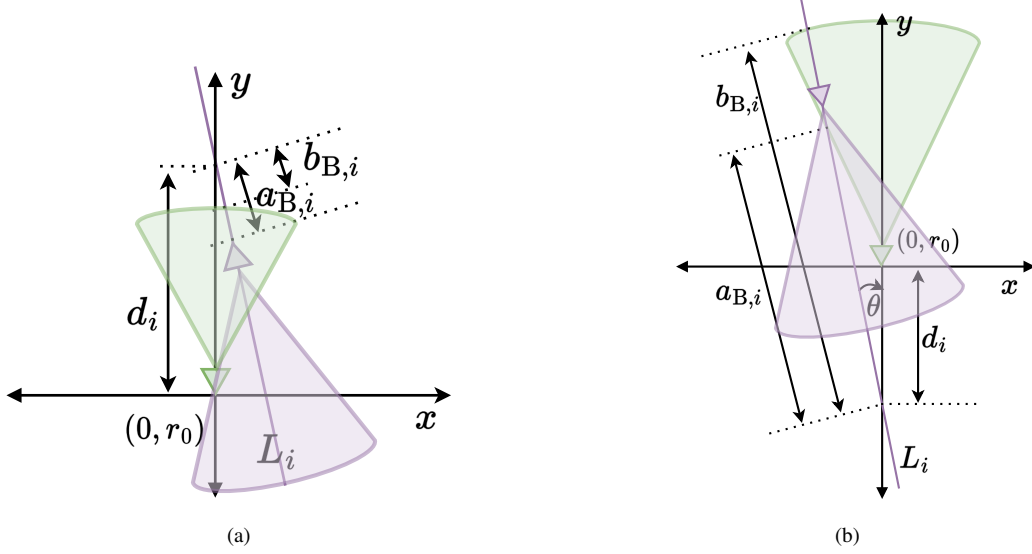


Fig. 10. (a) Case 2 with generating angle present in the first quadrant, and Case (3) with generating angle present in the third quadrant.

and $[A_7 \cup A_8]$ corresponding to scenario when the generating angle lies in the second, third and fourth quadrant. We now begin to derive the interfering distance, starting with case 1.

Case 1: Point of intersection occurs within the radar sector.

This case can be subdivided into two cases, which are:

Subcase (a): $0 \leq d_i \leq R_B$, and $\theta_i \in [0, 2\pi] \setminus \{[\Omega, \pi - \Omega] \cup [\pi + \Omega, 2\pi - \Omega]\}$. In this subcase, events $A_1 \cup A_4 \cup A_5 \cup A_8$ take place. Fig. 9a and 9b illustrates an example of this subcase, wherein the θ_i is generated in first quadrant i.e. $\theta_i \in A_1$. In this subcase, L_i intersects the curvature side of the radar sector. From Fig. 9b, we observe that the minimum interfering distance $a_{B,i}$ is calculated from point X to Y and would be negative, likewise maximum interfering distance $b_{B,i}$ is calculated from point X to V. The purple points represent the two end values of d_i . For simpler representation, XY represents the distance between points X and Y. Thus $a_{B,i}$ is then found as

$$\begin{aligned} a_{B,i} &= -XY = -(XZ - YZ) = -(d_i \cos \theta_i - OZ \cot \Omega) \\ &= -(d_i \cos \theta_i - d_i \sin \theta_i \cot \Omega). \end{aligned} \quad (16)$$

To determine $a_{B,i}$ for events $[A_4 \cup A_5 \cup A_8]$, we take the modulus of sine and cosine to accommodate all four quadrants. Likewise we can determine maximum interfering distance $b_{B,i}$ as

$$\begin{aligned} b_{B,i} &= XV = ZW - ZX = \sqrt{OV^2 - OZ^2} - ZX \\ &= \sqrt{R_B^2 - (d_i \sin \theta_i)^2} - d_i \cos \theta_i. \end{aligned} \quad (17)$$

Subcase (b): $0 \leq d_i \leq c_2$, and $\theta_i \in [0, 2\pi] \setminus \{[\Omega, \pi - \Omega] \cup [\pi + \Omega, 2\pi - \Omega]\}$. In this subcase events $A_2 \cup A_3 \cup A_6 \cup A_7$ take place. Fig. 9c and 9d illustrates an example of this subcase, wherein the θ_i is generated in first quadrant i.e. $\theta_i \in A_2$. In this subcase, L_i may intersect one of the edge lines or the circular arc portion of the radar sector. From Fig. 9d, we observe that the minimum interfering distance $a_{B,i}$ is calculated from point X to Y and would be negative, likewise maximum interfering distance $b_{B,i}$ is calculated from point Z to X. The minimum

interfering distance is found as

$$\begin{aligned} \sin \Omega &= \frac{ZY}{ZX} = \frac{d_i \cos(\theta_a)}{a_{a,i}} = \frac{d_i \cos(\frac{\pi}{2} + \Omega - \theta_i)}{a_{a,i}} \\ \therefore a_{B,i} &= \frac{d_i \sin(\theta_i - \Omega)}{\sin \Omega} \end{aligned}$$

In the above scenario where the interfering angle lies in the first quadrant, $\theta_a = \frac{\pi}{2} + \Omega - \theta_i$, and the same is found if θ_i lies in the third quadrant. But for the second and fourth quadrant $\theta_a = \frac{\pi}{2} + \Omega + \theta_i$. Also the modulus operator is applied in $d_i \sin(\theta_i - \Omega)$ and $d_i \sin(\theta_i + \Omega)$ to accommodate all four quadrants. Unlike $a_{B,i}$, where there are two different formulas for the first/third and second/fourth quadrant, we have two different formulas for $b_{B,i}$, but they depend on distance d_i . When $c_1 \leq d_i \leq c_2$, we see that line L_i will intersect only the circular arc portion of the radar sector; hence, the distance $b_{B,i}$ is the same as of subcase (a). For the case of $0 \leq d_i < c_1$, the line L_i does not intersect the circular arc, but one of the edge lines of the radar sector as shown in Fig. 9c and 9d. The distance $d_i = c_1$ represents the edge case when line L_i intersects simultaneously with the radar sector's circular arc and one of the edge lines. Therefore, for $d_i < c_1$, line L_i intersects only the border lines. Thus by solving $y = \cot \Omega + r_0$, $x \cos \theta_i + y \sin \theta_i = r_i$, and $x^2 + (y - r_0)^2 = R_B^2$ for y gives us the value of c_1 . And as usual, take the modulus of the trigonometric functions, which are functions of generating angles. The value of $b_{B,i}$ is then found as,

$$\begin{aligned} \tan \Omega &= \frac{VW}{d_i + WZ} = \frac{b_{B,i} \sin \theta_i}{d_i + b_{B,i} \cos \theta_i} \\ \therefore b_{B,i} &= \frac{d_i \tan \Omega}{\sin \theta_i - \tan \Omega \cos \theta_i} \end{aligned}$$

Now, for any $\theta_i \in \Theta$, c_2 is the maximum value of d_i , beyond which any none of the interfering radars can cause interference at ego radar and is found by solving,

$$c_2 \sin \theta_i \cot \Omega - c_2 \cos \theta_i \leq \sqrt{R_B^2 - (c_2 \sin \theta_i)^2} - c_2 \cos \theta_i.$$

Case 2: Point of intersection occurs outside the radar sector but ahead of ego radar. Here $d_i > R_B$, and $\theta_i \in [0, 2\pi] \setminus \{[\Omega, \pi - \Omega] \cup [\pi + \Omega, 2\pi - \Omega]\}$.

In this case, the intersection point lies ahead and outside the radar sector. This case arises only when event $A_1 \cup A_4 \cup A_5 \cup A_8$ take place. Fig. 10a illustrates a scenario of Case 2 i.e. $\theta_i \in A_1$, where we see that intersection is happening at a distance $d_i > R_B$. If we examine this scenario carefully, we notice that distance $a_{B,i}$, and $b_{B,i}$ are similar to earlier scenarios we have encountered in Case 1. The distance $a_{B,i}$ and $b_{B,i}$ is same as of distance given in (16) and (17) respectively, given in subcase(a). Although from Fig. 10a, it appears that $b_{B,i}$ is smaller than $a_{B,i}$, this is not the case. As the distance is measured from the perspective of the interfering point, both $b_{B,i}$ are negative such that $b_{B,i} > a_{B,i}$. Thus, by combining subcase (a) and case 2, we revise the range of d_i as $c_1 \leq d_i \leq c_2$.

Case 3: Point of intersection occurs outside the radar sector but behind the ego radar. Here $d_i < 0$, and $\theta_i \in [0, 2\pi] \setminus \{[\Omega, \pi - \Omega] \cup [\pi + \Omega, 2\pi - \Omega]\}$.

This is the third case that arises when the point of intersection is beyond ego radar. This case arises only when event $A_1 \cup A_4 \cup A_5 \cup A_8$ take place. Fig. 10b illustrates a scenario of Case 3, i.e., $\theta_i \in A_5$ when the intersection point lies behind the ego radar. The distance $b_{B,i}$ is the same as the distance given in (17), given in subcase(a), as L_i is intersecting the circular arc region of radar sector. The value of $a_{B,i}$ can be derived in a similar manner to how we derived the $b_{B,i}$ in subcase (a) and (b), we leave to the reader to work it out. Also, $d_i > c_1$ for the line L_i to have interfering radars.

This completes the proof of theorem 1 \square